High-temperature oxidation behavior of HiPIMS as-deposited Cr-Al-C and annealed Cr2AlC coatings on Zr-based alloy

Michael Ougier, Alexandre Michau, Fernando Lomello, Frédéric Schuster, Hicham Maskrot, Michel Schlegel

Version of Record: https://www.sciencedirect.com/science/article/pii/S0022311519309924
Manuscript_b0a6a1f77cc5e81a8823bce3b4e67644

High-temperature oxidation behavior of HiPIMS as-deposited Cr-Al-C and annealed Cr_2AlC coatings on Zr-based alloy

Michaël OUGIER[1], Alexandre MICHAU[1], Fernando LOMELLO[1], Frederic SCHUSTER[2], Hicham MASKROT[1], Michel L. SCHLEGEL[1]*

[1]Den–Service d'Etudes Analytiques et de Réactivité des Surfaces (SEARS), CEA, Université Paris-Saclay, 91191 Gif-sur-Yvette, France

[2]CEA Cross-Cutting Program on Materials and Processes Skills, 91191 Gif-sur-Yvette, France

** Corresponding author. E-mail address: alexandre.michau@cea.fr (A. Michau), CEA, Université Paris-Saclay, 91191 Gif-sur-Yvette, France*

Abstract

Protective coatings of Zr-based claddings have been proposed for the development of Accident Tolerant nuclear Fuel (ATF). Coatings forming stable oxides at high temperature such as MAX phases are attractive candidates for these applications. In this study Cr-Al-C coatings were deposited on coupons of Zr-based alloy (Zr702) by High Power Impulse Magnetron Sputtering (HiPIMS). Cr_2AlC coatings were then obtained by annealing of the as-deposited films at a temperature below metallurgical degradation of Zr alloys. The behavior of as-deposited Cr-Al-C and annealed Cr_2AlC coatings with respect to high-temperature oxidation slightly differ for short oxidation times but converge for longer durations. Oxidized coatings are made of (i) an external dense, covering, adherent and thin scale of aluminum and chromium oxides, (ii) an intermediate thicker, porous layer of chromium carbide and (iii) an interdiffusion layer. Both coatings are protective in dry and wet air (up to 1473 K for 2 h in air-28 % H_2O for an initial thickness of 7 µm), and are thermal shock-resistant. Self-healing capability is observed for submicronic defects. The top oxide scale acts as a barrier against oxygen diffusion, thus efficiently protecting the Zr702 substrate from extended oxidation

except near coupon edges. The results indicate that Cr-Al-C thin films grown by HiPIMS process and annealed Cr_2AlC coatings are both promising candidates for ATF cladding coatings.

Keywords: HiPIMS, Accident Tolerant Fuels, Cr_2AlC, MAX phase coating, high-temperature oxidation, self-healing

1 Introduction

In light water reactors (LWRs), uranium oxide or other fissile fuels are encased in metallic tubes or claddings. Claddings therefore represent a crucial safety component in LWRs, as they are the first containment barrier against dispersal of fission products. Zirconium alloys are widely used as fuel cladding material in LWRs owing to their transparency to neutrons, reasonable corrosion resistance in pressurized water conditions (up to 573 K, 155 bar [1]) and structural integrity under irradiation. However, the properties of Zr-based claddings are dramatically altered under the severe conditions of a loss of coolant accident (LOCA) [2, 3]. In the LOCA scenario, a rapid increase in temperature leads to zirconium oxidation and corrosion by high-temperature steam, resulting in cladding degradation and burst, along with dihydrogen release. Eventually, the nuclear core can partially melt and dihydrogen explode. To limit the impact of the high-temperature steam oxidation and to prevent dihydrogen generation during LOCA, accident-tolerant fuels (ATF) are now developed. One strategy is to replace the current Zr-alloys by materials exhibiting enhanced oxidation resistance, mainly SiC-SiC composites [4, 5], or Mo or FeCrAl alloys [6, 7]. These long-term solutions require prolonged developments and qualification efforts. An alternate approach is to protect the Zr alloy of current fuel claddings with coatings. To this end, most studies are focusing on metallic coatings and specifically Cr [8-12]. Chromium performs well under high-temperature oxidation conditions thanks to the formation and growth of a protective Cr_2O_3 scale. However, Cr_2O_3 becomes unstable when exposed to steam at temperatures above 1473 K [13]. Another concern is the behavior of Cr-coated Zr-based cladding beyond the Cr-Zr eutectic point, which occurs around 1600 K. This eutectic formation could lead to the embrittlement of the cladding [11, 14]. Other coating materials and architectures are investigated like carbon-based coatings [15, 16], metallic alloys [17-19], ceramics including oxides [20], nitrides [21, 22], composites or multilayers coatings [8, 23, 24] and nanolaminated ceramics such as MAX phases [25-30].

The MAX or $M_{n+1}AX_n$ phases (where 'M' stands for an early transition metal element, 'A' is an element of the A group, mostly from the IIIA and IVA columns of the periodic table, and 'X' is C or N) are hexagonal ternary carbides or nitrides with a nanolayered structure, resulting in a unique combination of both metal and ceramics properties [31-33]. The various MAX stoichiometries are often referred to as 211 (for n = 1), 312 (n = 2), and 413 (n = 3). Aluminium-containing MAX phases, for example Cr_2AlC, possess excellent high-temperature oxidation resistance both in air and steam due to the formation of a continuous, dense and adherent alumina scale [34, 35]. This external layer can withstand higher temperatures in steam before volatilization compared to chromia [36, 37]. In addition, Al atoms easily diffuse from the MAX phases structure at elevated temperatures and oxidize to form Al_2O_3 in cracks and other defects, thereby obstructing these voids according to a self-healing process [38-40]. Finally, MAX phases display reasonable radiation tolerance [41-43]. Reported studies show that their behavior under irradiation depends on the elements and exact stoichiometry of the respective phases along with the initial microstructure [44-50].

Thin films made of MAX phases have been successfully synthesized by various physical vapor deposition (PVD) techniques like magnetron sputtering [51-55] and cathodic arc evaporation [56, 57]. Moreover, in order to obtain thin films of fairly crystalline Ti-based MAX phases, quite high temperatures or additional heat treatments (typically $\geq$ 873 K) are needed [58-60]. These temperatures are greater than the recommended upper limit of 853 K imposed on Zr-based alloys to avoid metallurgical degradation [61]. In keeping with this constraint, crystalline or partially crystalline Cr_2AlC films have been obtained under 823 K with PVD techniques. The (micro)crystalline phases were obtained either directly in a heated deposition chamber or on a heated substrate-holder [53, 62-65], or by growing the coating without intentional heating and by performing an annealing afterwards [66-68]. The deposition of Cr_2AlC protective films for ATF may be further optimized by using high power impulse magnetron sputtering (HiPIMS). First, the HiPIMS plasma delivers a high energy

flux of ionic metallic species [69, 70] which can enhance surface mobility of species on the growing films, and so improve structural reorganization at the growth surface. This would favor the formation of pure, well crystallized 211 MAX phases below the highest temperatures allowed for work on the last generations of Zr alloys, as reported for Cr_2AlC and V_2AlC [55, 71]. Second, despite lower growth rates, superior properties are often reported for some materials deposited by HiPIMS compared to direct current (DC) magnetron sputtering, especially regarding protective applications (denser, smoother and better adhesive coatings) [72-74].

In this study, Cr-Al-C thin films were deposited on Zr-based alloy (Zr702) by HiPIMS from a Cr_2AlC compound target and subsequently annealed. The composition, structure and behavior of as-deposited and annealed coatings are investigated at high temperatures in dry and wet air. The results provide an insight into the oxidation mechanisms and the protective effects of the coatings grown by HiPIMS. A comparison is made for some oxidation tests with a reference system consisting of Cr deposited by HiPIMS.

2 Material and methods

2.1 Cr-Al-C and Cr film growth

Briefly, Zr702, stainless steel (SS304L) and monocrystalline silicon flat substrates were used in this work. Centimetric-size Zr702 coupons (30×20×2 mm) with a suspension hole were ground with SiC paper up to 2000 grit and ultrasonically cleaned in water, acetone and alcohol. Cr-Al-C and pure Cr coatings were grown using an in-house PVD-HiPIMS equipment developed by DEPHIS (Etupes, France) equipped with two cathodes and a sample holder with a triple rotation axis. Zr702 coupons were dangling from hooks of the sample holder. A Cr_2AlC composite target (560×150×10 mm) with a Cr:Al:C stoichiometry of 2:1:1 (99.9%) synthesized by hot pressing (Neyco Vacuum & Materials) was mounted and sputtered. X-ray diffraction (conditions given below) showed that the target material corresponds to crystalline Cr_2AlC, with no detected contribution from other crystalline phases

(Fig. 1a). A Cr target (99.8% purity; Nano&Micro PVD) with the same dimensions was used for reference Cr coatings. Unipolar pulse was applied to the targets using a DC power supply from ADL GmbH (10 kW GX100/1000) combined with a MELEC HiPIMS pulse controller (SPIK2000USB Dual) operated in a power-controlled mode. Substrates were etched prior to deposition in order to remove contaminants and improve adhesion of coatings. For this etching step, the Cr target was sputtered under HiPIMS regime (target voltage 950 V, pulse frequency 1923 Hz and pulse width 20 µs for an average power of 3000 W) in a 0.5 Pa Ar atmosphere for 10 min. A negative bias of -900 V was applied to the sample holder. After etching, Cr-Al-C coatings were deposited in 0.35 Pa Ar and substrates were left at a floating bias potential. The average power, pulse width and frequency were 2500 W, 70 µs, and 310 Hz, respectively. These parameters resulted in a peak power density of 280 W/cm^2 and a duty cycle of 2.2%. The vacuum chamber was heated by two radiant heaters up to 673 K. A constant temperature was maintained during film growth. The Cr coatings were deposited under Ar at 0.7 Pa and the substrates were biased at -150 V. The target was operated in HiPIMS mode with the following parameters: pulse width of 50 µs at a frequency of 500 Hz and average power of 3500 W.

Coating crystallization was promoted by an ensuing annealing step. Coated samples were loaded in a horizontal alumina tube furnace (Carbolite; Gero 301 PID controller) at room temperature, then heated to 823 K at a heating rate of 4 K/min and were held for 4 h at 823 K in Ar (99.9999%). After 4 h, samples cooled down to room temperature in the oven. In the following paper, Cr-Al-C refers to as-deposited coatings, and Cr_2AlC refers to annealed films.

2.2 Oxidation tests

To evaluate the performances of Cr_2AlC as an ATF coating material, two oxidation tests were performed on coupons (uncoated or coated on all faces with as-deposited and annealed coatings). In a first approach (test #1), isothermal oxidations were conducted at 1373 K under static air in a muffle furnace. Samples were loaded in the furnace pre-heated at 1373 K, and

were baked for different oxidation times (15, 30 and 60 min). Samples were then rapidly removed and directly quenched in ambient water.

The second oxidation test (test #2) consisted in thermogravimetric analyses, using a TGA16 system (Setaram) coupled with a humidity generator (Wetsys; Setaram) for experiments in humid air. Humid air generation was prepared at 343 K with a relative humidity of 90 %, resulting in 28 vol. % H_2O content (hereafter called wet air). Samples were hung to a Pt wire and heated from room temperature to 1473 K at a rate of 10 K/min under dry and wet air with a flow rate set to 38 mL/min. They were kept at 1473 K for 10 min. Mass changes were monitored during the entire thermal cycle.

2.3 Structural and chemical characterization

The surface, cross section morphology, and composition of the as-deposited and annealed coatings before and after oxidation experiments were investigated by scanning electron microscopy (SEM) equipped with a field emission gun (JEOL JSM7000-F) operated at 15 kV with a beam current of 2 nA and coupled with an energy dispersive X-ray (EDX) spectrometer (Bruker XFlash 5010) for quantitative analysis. Crystallographic structures of the Cr_2AlC target material and of the coatings were investigated by X-ray Diffraction (XRD; Bruker D8 Discover) using Cu K_α radiation with a fixed angle incident beam (1 or 5° with respect to the sample plane). Raman spectra were collected on a LabRam HR spectrometer (Horiba Jobin Yvon). A frequency-doubled Nd-YAG laser (wavelength of 532 nm) was used as source. Chemical compositions of the coatings were measured by Glow Discharge Optical Emission Spectroscopy (GDOES; Horiba GD-Profiler 2™).

3 Results

3.1 Characterization of as-deposited and annealed Cr-Al-C coating

A weak and diffuse contribution around 42° is detected on the XRD pattern of the as-deposited Cr-Al-C coating, characteristic of nanocrystalline materials (Fig. 1a). The formation of nanocrystals or of metastable solid solutions were already observed for substrate

temperatures too low to form well crystallized MAX phases [52, 55, 67, 75]. After annealing at 823 K for 4 h in Ar, the presence of Cr_2AlC in the films was confirmed by detection of relevant diffraction peaks (Fig. 1a). The annealed coating has a preferred orientation along the (006) axis with a texture coefficient of 3.5 (calculated according to the equation given in [76] with the reference PDF-00-058-0267 phase). Compared to the XRD pattern of the target material, the only missing reflection is (002) around 13°, probably hidden in the baseline. There is no evidence of the formation of any other phase such as carbides or intermetallic compounds.

Raman spectra of as-deposited and annealed samples were compared to that of the Cr_2AlC target in Fig. 1b. The 150 to 400 cm^{-1} wavenumber range contains typical peaks for $M_2A_1X_1$ phases. Attribution of the Raman bands was based on theoretical prediction of the Raman spectra [45, 77-82]. For theoretical Cr_2AlC spectra, four Raman active optical modes, noted 1a to 1d, were expected. The second and third contributions (1b and 1c) are usually overlapping in experimental data [45, 79-82]. Three bands are visible on the Raman spectrum of the HiPIMS target around 155 cm^{-1} (1a), 245 cm^{-1} (1b and 1c) and 335 cm^{-1} (1d) which are in agreement with the prediction. The as-deposited coating shows only a very broad hump around 220 cm^{-1}. After annealing for 4 h in Ar, this hump is still present and two bands appear at Raman shifts corresponding to the 1b (mixed with 1c) and 1d contributions. The evolution of the Raman spectra from the as-deposited to the annealed coatings supports the partial crystallization of Cr_2AlC MAX phase, as observed in XRD.

The SEM micrographs of cross-sections from the as-deposited coating on silicon and the annealed coating on Zr702 are shown in Fig. 2. The microstructure of as-deposited coatings consists in a dense packing of columns of about 100 nm wide (Fig. 2a). After annealing, the columns are still present, and a fine and submicronic structure is visible (Fig. 2b). Moreover, a 300 nm thick layer of distinct electron density (brightness on SEM images in back-scattered electron mode) appears on all annealed samples at the interface between the coating and the

Zr702 substrate. We attribute the formation of this layer to interdiffusion between the coating and the substrate during annealing. Interdiffusion of Cr, Al, C and Zr over distances of about 100 nm across the interface was further supported by GDOES measurements (data not shown). This results from the high chemical activity of Al in the coating as well as the high solubility of Al and Cr in Zr [35, 83].

Generally, coating thicknesses are homogeneous on Si substrates while they show small variations, mainly at the edges, on Zr702 coupons. It is worth noticing that no delamination and no spallation occurred for both as-deposited Cr-Al-C and annealed Cr_2AlC coatings. EDX and GDOES analyses of as-deposited and annealed coatings yield an average chemical composition of 48-52 at. % Cr, 23-25 at. % Al, and 24-27 at. % C, close to the stoichiometry of Cr_2AlC.

3.2 High-temperature oxidation behavior

3.2.1 Test #1 for 15 minutes on as-deposited and annealed coatings

During tests of isothermal oxidations in static dry air at 1373 K for 15 minutes followed by quenching in room temperature water, three phases crystallized in different proportions for as-deposited and annealed coatings, as shown in XRD (Fig. 3a). Two different oxidation products were detected in oxidized as-deposited coatings, i.e. Cr_2O_3 and α-Al_2O_3. The most important XRD contribution could however be attributed to Cr_7C_3. In contrast, in annealed films, α-Al_2O_3 was the only oxide present in significant amounts (Fig. 3a). Peaks characterizing the Cr_2AlC MAX phase disappeared and Cr_7C_3 was the main detected phase. Micro-Raman analysis of oxidized as-deposited coatings (Fig. 3b) yielded only one major contribution at 562 cm^{-1}, corresponding to Cr_2O_3 [84, 85], and no Al_2O_3 was observed. Five bands at 375, 415, 575, 645 and 748 cm^{-1} characteristic of Al_2O_3 and one band at 490 cm^{-1} associated to aluminium oxyhydroxide (bohemite or γ-AlOOH) were observed for the oxidized annealed coatings [86-90].

Fig. 4 superimposes SEM cross-sections with GDOES depth profiles for as-deposited and annealed coatings after oxidation. For all oxidized coatings, three distinct layers can be observed. First, a thin and dense layer of oxide scale covers the top of the coating. Second, a thicker and porous non-oxidized layer composed mainly of Cr and C coincides in position with the coating. Finally, a dense layer is observed in contact with the Zr702 substrate, and results from the interdiffusion of the elements between the coating and the substrate. No significant O uptake is detected in the (Cr,C) layer, the interdiffusion layer and the Zr702 substrate. GDOES measurements and complementary EDX mappings suggest the formation of an (Al,Cr,O) fringe at the surface of the oxidized as-deposited film (Fig. 4a), confirming XRD results. It is worth noticing that profiles of Cr and Al concentrations present local maxima in the top oxide layer which are not located at the same depth. On the other hand, the oxidized top layer of annealed coatings (Fig. 4b) contains mostly Al and O with a minor amount of Cr. It also appears that the (Cr,C) layer contains a minor Al content of about 10 at. %. Finally, C has diffused deeper in the Zr702 substrate than Cr and Al.

Micro-cracking was observed at the surface of the coatings and was attributed to water quenching following isothermal oxidation. However, the coatings remained adherent during the whole treatment and did not show any sign of spallation. Micro-cracking phenomena released internal stresses that were introduced during the growth of the films by HiPIMS (intrinsic and thermal stresses) and quenching (thermal stresses). Thermal stresses originate from contrasted thermal expansion of the substrate and the coatings over the investigated temperature range. Most cracks and the underlying substrate are not oxidized, confirming that they formed after the high-temperature test. However, in some locations, cracks cross-cutting the coatings down to the substrate are observed (Fig. 5a,b). The inner surface of these cracks is covered by the same oxide as the top oxide layer, meaning they formed before the oxidation test. A restricted volume (no more than 10 µm deep) of the Zr702 substrate is locally enriched with N, as revealed by EDX analysis (not shown here). Thus, the occurrence of nitridation

means that remaining nitrogen (from air) diffuses through the imperfections in the coating to the metal/coating interface, reacts with zirconium and forms nitrides, such as ZrN. It is worth noticing that nitrogen in the oxidizing atmosphere results in significantly stronger degradation of the cladding material than oxidation in pure oxygen or steam [91-93].

When surface damage is larger (as shown in Fig. 5c,d), the substrate is significantly more oxidized (up to 150 µm deep). This difference suggests that the dense and covering oxide scale on as-deposited and annealed coatings grows until a certain extent, depending on the aggressive atmosphere. A small defect, < 1 µm in our case, can be clogged, *i.e.* self-healed, preventing further degradation. This behavior is consistent with previous studies on Cr_2AlC [38], and illustrates the self-healing capability of the MAX phase coating.

3.2.2 Test #1 for 30 and 60 minutes on annealed coatings

After 30 and 60 minutes in static dry air at 1373 K followed by water quenching, α-Al_2O_3, Cr_2O_3 and Cr_7C_3 are detected (Fig. 6). Moreover, ZrO_2 is identified after 30 minutes of oxidation and its contribution increases for 60 minutes, suggesting that the substrate is partially oxidized. This results from premature failure of the thinner coating at the edges of our rectangular coupons [66]. Coating spalling is also visible on the edges of the hole drilled into the coupons (Fig. 8). The hole clearly acts as a weak point, from which oxidation of the Zr702 substrate propagates. The increase in amount of Cr_2O_3 is also evident, whereas Cr_7C_3 contribution decreases with increasing oxidation time. This indicates the gradual oxidation of the chromium carbide layer. Finally, the XRD contribution of α-Al_2O_3 decreases with an increasing oxidation time.

Fig. 7 compares the microstructural and architectural evolution of annealed Cr_2AlC coatings (Fig. 7a-c) and reference Cr coatings (Fig. 7d-f) during test #1 for 15 and 60 minutes. Annealed Cr_2AlC and reference Cr coatings had initial thicknesses around 3 and 15 µm, respectively. After 60 minutes the architecture of the oxidized annealed Cr_2AlC coating is similar to 15 minutes, *i.e.* (i) a thin top oxide scale (~ 400 nm), (ii) a thicker and porous

(Cr,C) layer (~ 2 µm) and (iii) a dense interdiffusion layer (~ 800 nm) near the substrate surface. According to EDX mappings, XRD patterns, and GDOES profiles, the top oxide scale is made first of α-Al_2O_3 and then of a mixture of α-Al_2O_3 and Cr_2O_3. The top oxide scale is adherent and dense. The porous (Cr,C) layer has Al, C and Cr contents (measured by GDOES) of around 10, 28, and 62 at. %, respectively, which gives a Cr:C ratio of 2.2, very close to the ratio 2.3 for the Cr_7C_3 phase detected by XRD. Finally, GDOES analysis and SEM observations also show the mutual exclusion of Zr and O over most of the surface, meaning that the ZrO_2 contribution in XRD patterns of oxidized coatings corresponds to the oxidation of the substrate around the sample edges only.

A succession of three layers is observed for Cr coatings after 15 and 60 minutes (Fig. 7d-f). They consist in a top covering and dense Cr_2O_3 layer. It is however brittle and less adherent for similar thicknesses than the top oxide scale of Cr_2AlC. The thickness of this Cr_2O_3 film increases with oxidation time at the expense of the underlying non-oxidized Cr layer. About 5 µm of Cr is left after an oxidation time of 60 minutes, *i.e.* one third of the initial thickness. An interdiffusion layer between Zr and Cr is also observed. This interphase is four times thicker than for Cr_2AlC coatings according to SEM observations. GDOES profiles confirmed this extended diffusion of Cr in the substrate, with an amount of 10 at. % Cr measured even 15 µm below the substrate surface. On the other hand, for the oxidized annealed Cr_2AlC coating, the 10 at. % threshold is reached at 500 nm below the substrate surface. Unlike Cr_2AlC coatings, ageing of the Cr coating leads to the formation of a limited amount of porosities, concentrated at the interface between the Cr and the interdiffusion layer.

3.2.3 Test #2 on as-deposited coatings

Mass gains of uncoated and coated Zr702 coupons were measured by TGA during a heating ramp and an isothermal oxidation step under dry and wet air at 1473 K (Fig. 8). Coated coupons consisted of as-deposited Cr-Al-C coatings with a thickness of 7 µm and a reference Cr coating with a thickness of 15 µm. Final mass gains for coated samples (2 to 5 $mg.cm^{-2}$)

are about five times smaller than for uncoated Zr702 (23 to 28 $mg.cm^{-2}$) under both atmospheres. Moreover, Cr and as-deposited Cr-Al-C delay runaway oxidation of the Zr702 substrate for 50 minutes, corresponding to a temperature higher by 400 K. Furthermore, the mass gain of coated samples is mostly caused by substrate oxidation around the suspension hole, due to peeling after local failure of thinner and inhomogeneous coating (*e.g.* Fig. 8). It appears that the mass gain is lower in wet air, suggesting lower oxidation rates, as reported elsewhere [94].

SEM cross-sections after test #2 in dry air show that uncoated Zr702 was strongly deteriorated by oxidation with the formation of an 80 µm-thick porous ZrO_2 layer. In contrast, the underlying substrate of the coated sample is not oxidized, except in the vicinity of coupon edges and hole. As for the test #1, the surface of the oxidized, as-deposited coating is mostly made of a mixture of Al and Cr oxides.

An additional high-temperature oxidation test for an as-deposited Cr-Al-C coated sample (7 µm of initial thickness) was performed for nearly 2 h at 1473 K in wet air. The SEM micrograph shows that the coating segregates into three sublayers as previously described (Fig. 9). The top oxide layer is still dense and adherent even after 2 h. However, the metallographic preparation for the microstructural observations induced partial spalling of this top layer. We deduced from XRD analyses, EDX mappings and GDOES analyses that this top layer is a mixture of α-Al_2O_3 and Cr_2O_3. Interestingly, most of the porosities in the intermediate (Cr,C) layer disappear after prolonged oxidation, as they are filled by oxides, probably α-Al_2O_3 and Cr_2O_3. The GDOES analyses (Fig. 9) show that the (Cr,C) layer is now depleted in C (5 to 7 at. %) and is mainly composed of Cr (50 to 60 at. %), Al (15 to 20 at. %) and O (10 to 15 at. %). The third subunit corresponds to an approximately 1.8 µm thick interdiffusion layer formed at the substrate/coating interface. Solid phases in the interdiffusion layer could not be identified with our XRD setup, either because of their poor crystallinity and low mass fraction or because of the limited penetration depth of X-rays. Deeper in the

substrate, the GDOES depth profiles reveal subsurface enrichment of C. This observation suggests the possible formation of a zirconium carbide phase in the interdiffusion layer, as previously observed for a chromium carbide coating (composition of $Cr_{0.64}C_{0.33}O_{0.03}$) grown on a Zr-based alloy after an oxidation at 1473 K for 10 min in steam [95]. Oxygen amounts are negligible inside the Zr702 substrate, except in oxidized areas near the edges and the hole. Finally, Zr702 has undergone metallurgical transformation due to the high temperatures.

4 Discussion

4.1 Oxidation of the as-deposited Cr-Al-C and annealed Cr_2AlC coatings

The corrosion interfaces for as-deposited Cr-Al-C and annealed Cr_2AlC MAX-phase coatings exhibit a similar architecture after a long period of oxidation at high temperature in air. Part of the similarity can be explained by the fact that the high corrosion temperatures ($\geq$ 823 K, the annealing temperature in our study) also promote partial crystallization and ordering of the as-deposited coating [67, 96]. However, the oxidation behavior of these two coatings displays significant differences.

During the initial stage of oxidation (typically between 15 and 30 minutes), a mixture of Al and Cr oxides forms at the top surface of the as-deposited Cr-Al-C coating while a continuous and dense layer of α-Al_2O_3 only appears on the surface of the crystalline annealed Cr_2AlC coating. For longer oxidation time (in our case, 30 minutes at 1373 K in air), Cr_2O_3 eventually forms in the top oxide layer of annealed Cr_2AlC coatings. This contrasted oxidation behavior of the M and A elements from the MAX phase was observed for the Ti_2AlC phase system. In that case, Ti-Al-C thin films were synthesized on alumina substrates by HiPIMS without intentional heating, and then some of the films were annealed to promote the formation of Ti_2AlC [97]. After 5 h at 1073 K in air, the authors reported the growth of TiO_2 and Al_2O_3 for as-deposited Ti-Al-C coatings and only Al_2O_3 for annealed Ti_2AlC films. TiO_2 crystallized in the annealed Ti_2AlC coating after 20 hours of oxidation. The different oxidation behavior between Ti-Al-C and Ti_2AlC coatings was assigned to dissimilar values of the

thermodynamic activity for Al in the amorphous coatings and in the crystalline Ti_2AlC MAX phase films. In our study, we expect that the microstructure and texture of annealed crystallized Cr_2AlC films may influence on the oxidation behaviour relative to the nanocrystalline as-deposited Cr-Al-C coatings.

As far as Cr_2AlC is concerned, the preferential growth of Al_2O_3 over Cr_2O_3, on the surface of bulk and coated samples at temperatures above 973 K was extensively investigated [66, 96, 98-103]. Thermodynamic considerations support the experimental observations regarding bonding energies for Al-Cr and Cr-C bonds in Cr_2AlC along with Gibbs free energies of Al_2O_3 and Cr_2O_3 formation. For phases of M_2AX composition such as Cr_2AlC, the crystal structure consists of M octahedral sheets with X atoms filling the octahedral sites; these sheets are bound by planar closed-packed A atomic interlayers [104]. In Cr_2AlC, the metallic Cr-Al bonds are weaker than the covalent Cr-C bonds [105, 106], implying that Al atoms diffuse outward of the crystal structure more easily than Cr.

In our case, the oxidation of as-deposited of Cr-Al-C and annealed Cr_2AlC coating in air at 1373 K resulted in the formation of an oxide scale covering a porous (Cr,C) layer. For as-deposited Cr-Al-C coatings, Al and Cr probably migrated simultaneously to the surface of the coatings to form a mixed (Al,Cr) oxide layer. For annealed Cr_2AlC coatings, Al initially migrated to form a passivating layer of Al_2O_3. The XRD signal and Cr:C ratio of the porous (Cr,C) layer are characteristic of Cr_7C_3. It is likely that other Cr carbides as Cr_3C_2 crystallized during oxidation, as reported by several authors [102, 103] but they were not detected in our experiments. Moreover, the Cr_3C_2 phase has not been observed after an oxidation at 1372 K, probably because it decomposed to form Cr_7C_3 (s), CO (g), CO_2 (g) and Cr_2O_3 (s) [107-109]. Furthermore, it has been shown that the release of CO or CO_2 gas during oxidation of carbides such as SiC and Cr_3C_2 resulted in the formation of cavities [110-112]. Nonetheless, no porosity in the carbide layer of massive Cr_2AlC specimens was observed for the same oxidation conditions [34, 98-100, 103]. In contrast to the Cr_2AlC coatings, it is reasonable to

assume that bulk Cr_2AlC samples have a significantly larger supply of Al available for diffusion within the near surface region of the MAX phase to avoid significant depletion and disruption of the passivating layer over the duration of corrosion experiments.

The porosity increase of the carbide layer with oxidation time suggests that pore development is likely a consequence of diffusion processes with distinct kinetics and starting times. At the initial stage of oxidation, outward diffusion of Al firstly generates rapid growth of a protective alumina layer at surface, meanwhile, the Cr_2AlC lattice distorts and transforms into (Cr,C) phases under oxide scale. Secondly, with the growth of alumina layer, Al is migration out of the coating leads to further degradation of the Cr_2AlC MAX phase into (Cr,C) phases. When Al depletion reaches a critical threshold, inward diffusion of O through the alumina scale oxidizes the (Cr,C) layer. It is then likely that O reacted with C to form gaseous compounds like CO or CO_2 with Cr_7C_3 and Cr_2O_3 [103]. The release of CO_2 together with the outward diffusion of Al and Cr contribute to the formation of a porous sublayer. The presence of Cr_2O_3 in the top oxide scale could lead to an accelerated degradation mechanism since Cr oxides form volatile hydroxides that can evaporate at high temperatures in H_2O-containing atmospheres with higher rates compared to alumina [36, 113].

Additionally, interdiffusion of elements from the coatings and the Zr702 substrate at high temperature (during oxidation) leads to the formation of a specific interphase layer.

Interestingly, some micro-cracks present before the oxidation tests completely disappeared after high-temperature oxidation. This is probably because of the self-healing capabilities of Cr-Al-C and Cr_2AlC coatings at high temperatures, owing to the high diffusivity of Al, and the formation of dense, stable and adhering Al_2O_3 scale with a high relative volume expansion [114]. This self-healing was efficient for submicronic defects but ineffective for larger cracks, probably because Al supply was too limited. Our results thereby corroborate high-temperature crack-healing behavior observed for the bulk Cr_2AlC or other MAX phases [40, 115] and in previous studies of Cr_2AlC films [38, 66].

4.2 Protective effect of the coating on Zr702

The main objective of our coating is to hinder high-temperature oxygen diffusion into the substrate to prevent devastating damage. One common strategy is the use of coatings favoring the formation of a sealing, dense, stable and adherent protective scale of oxide. Unprotected Zr702 was significantly oxidized in the temperature range and time intervals investigated in our study. In contrast, Zr702 protected by Cr-Al-C and Cr_2AlC coatings remained undamaged, except at coupon edges. The degradation of coated Zr702 during high-temperature oxidation is supposed to start when the top oxide scale loses its protecting properties. This loss was not observed even after one hour in dry air at 1373 K and two hours in wet air at 1473 K.

The most likely scenario for the degradation of the coatings is Al depletion within the top oxide layer. The Al depletion can result from diffusion processes either inwards the substrate (Al interdiffusion with the Zr702 substrate) or outward the coating (Al diffusion and oxidation within the top scale). One solution to mitigate inward interdiffusion during annealing is the insertion of a suitable diffusion barrier. In addition to diffusion considerations, this barrier layer should be selected in order to prevent the formation of intermetallic brittle phases at any temperatures likely to be reached.

The Al depletion will also result in the accumulation, in the surface oxide scale, of Cr oxide with less favorable protective properties under high-temperature oxidative conditions. Moreover, the diffusion of Al, Cr and C to the top oxide scale and inside the substrate is deleterious to protective properties since it creates pores within the intermediate (Cr,C) layer, as previously reported [103]. Undeniably, porosities potentially constitute a shortcut for oxygen diffusion to the substrate.

We should also keep in mind that LOCA occur with high-temperature water steam that has a very particular chemistry. Thus, degradation mechanisms in high-temperature steam may be different from the ones identified in (wet) air. Indeed, the oxidation in steam for 1 h at 1273 K

of a Cr_2AlC coating grown on Zircaloy-4 substrates indeed led to the formation of only an Al_2O_3 scale without Cr_2O_3 [66].

5 Conclusions

In this study, dense and nanocrystalline Cr-Al-C coatings were deposited by HiPIMS and the MAX phase Cr_2AlC coatings were obtained by subsequent thermal annealing. Coated samples were then subjected to several high-temperature oxidation tests.

As-deposited Cr-Al-C and annealed Cr_2AlC coatings protect Zr702 substrates from oxidation in dry or wet air at high-temperature (up to two hours at 1473 K in wet air for a 7 µm thick coating) owing to the growth of a continuous, dense and adherent top oxide scale, which acts as a barrier against oxygen diffusion. This layer is first made of α-Al_2O_3 and Cr_2O_3 for as-deposited Cr-Al-C coating while only α-Al_2O_3 is present for annealed Cr_2AlC coating. For longer oxidation durations, the top oxide layer is made of Al and Cr oxides for both coatings, a consequence of Al depletion from the coating. The outward diffusion of Al and Cr to the top oxide layer and the inward interdiffusion of Cr, Al and C with Zr at the substrate-coating interface leaves a porous intermediate chromium carbide Cr_7C_3 layer. Further degradation of the coatings is expected for prolonged oxidation times after the full oxidation of the (Cr,C) middle layer or loss by interdiffusion.

To extend the coating lifetime at elevated temperatures, greater thicknesses and appropriate diffusion barriers between the coating and the Zr substrate should be considered. However, the thickness of protective coatings on the surface of Zr-based claddings should be limited to avoid significant impact on the neutron transport in LWRs.

We have not yet assessed the performance of our coatings under normal operation conditions of a LWRs, *i.e.* the chemical stability and radiation resistance of the coating in aqueous electrolytes at 633 K. Nevertheless, previous studies of bulk Cr_2AlC corrosion showed little change under simulated primary water conditions [28]. The coating lifetime in LWR nominal conditions can be improved by addition of a thin top layer made with a material that does not

form an unstable oxide in aqueous environment, such as Cr. In addition, new oxidation experiments at higher temperature and in pure flowing steam more representative of LOCA conditions are desirable. The results reveal the possibilities for the application of Cr-Al-C based coatings as ATF cladding materials.

Acknowledgements

This work was funded by the CEA Cross-Cutting program on Advanced Materials. J. Varlet and K. Ginestar are thanked for their assistance in sample preparation. E. Monsifrot and D. You are warmly thanked for their remarks and suggestions. The authors want to acknowledge M. Tabarant and S. Bosonnet for their contribution in sample analysis and constructive discussions.

References

[1] K.A. Terrani, S.J. Zinkle, L.L. Snead, Advanced oxidation-resistant iron-based alloys for LWR fuel cladding, Journal of Nuclear Materials 448(1-3) (2014) 420-435.

[2] J.C. Brachet, L. Portier, T. Forgeron, J. Hivroz, D. Hamon, T. Guilbert, T. Bredel, P. Yvon, J.P. Mardon, P. Jacques, Influence of hydrogen content on the alpha/beta phase transformation temperatures and on the thermal-mechanical behavior of Zy-4, M4 (ZrSnFeV), and M5 (TM) (ZrNbO) alloys during the first phase of LOCA transient, in: G.D. Moan, P. Rudling (Eds.), Zirconium in the Nuclear Industry: Thirteenth International Symposium, American Society Testing and Materials, W Conshohocken, 2002, pp. 673-700.

[3] L. Portier, T. Bredel, J.C. Brachet, V. Maillot, J.P. Mardon, A. Lesbros, Influence of long service exposures on the thermal-mechanical behavior of Zy-4 and M5 (TM) alloys in LOCA conditions, in: P. Rudling, B. Kammenzind (Eds.), Zirconium in the Nuclear Industry: 14th International Symposium, American Society Testing and Materials, W Conshohocken, 2005, pp. 896-920.

[4] K. Shapovalov, G.M. Jacobsen, L. Alva, N. Truesdale, C.P. Deck, X. Huang, Strength of SiC_f-SiC_m composite tube under uniaxial and multiaxial loading, Journal of Nuclear Materials 500 (2018) 280-294.

[5] C.P. Deck, G.M. Jacobsen, J. Sheeder, O. Gutierrez, J. Zhang, J. Stone, H.E. Khalifa, C.A. Back, Characterization of SiC–SiC composites for accident tolerant fuel cladding, Journal of Nuclear Materials 466 (2015) 667-681.

[6] B. Cheng, Y.-J. Kim, P. Chou, Improving Accident Tolerance of Nuclear Fuel with Coated Mo-alloy Cladding, Nuclear Engineering and Technology 48(1) (2016) 16-25.

[7] Y. Yamamoto, B.A. Pint, K.A. Terrani, K.G. Field, Y. Yang, L.L. Snead, Development and property evaluation of nuclear grade wrought FeCrAl fuel cladding for light water reactors, Journal of Nuclear Materials 467 (2015) 703-716.

[8] D.J. Park, H.G. Kim, Y.I. Jung, J.H. Park, J.H. Yang, Y.H. Koo, Behavior of an improved Zr fuel cladding with oxidation resistant coating under loss-of-coolant accident conditions, Journal of Nuclear Materials 482 (2016) 75-82.

[9] H.-G. Kim, I.-H. Kim, Y.-I. Jung, D.-J. Park, J.-Y. Park, Y.-H. Koo, Adhesion property and high-temperature oxidation behavior of Cr-coated Zircaloy-4 cladding tube prepared by 3D laser coating, Journal of Nuclear Materials 465 (2015) 531-539.

[10] J.-H. Park, H.-G. Kim, J.-y. Park, Y.-I. Jung, D.-J. Park, Y.-H. Koo, High temperature steam-oxidation behavior of arc ion plated Cr coatings for accident tolerant fuel claddings, Surface and Coatings Technology 280 (2015) 256-259.

[11] J. Bischoff, C. Delafoy, C. Vauglin, P. Barberis, C. Roubeyrie, D. Perche, D. Duthoo, F. Schuster, J.-C. Brachet, E.W. Schweitzer, K. Nimishakavi, AREVA NP's enhanced accident-tolerant fuel developments: Focus on Cr-coated M5 cladding, Nuclear Engineering and Technology 50(2) (2018) 223-228.

[12] B. Maier, H. Yeom, G. Johnson, T. Dabney, J. Walters, J. Romero, H. Shah, P. Xu, K. Sridharan, Correction to: Development of Cold Spray Coatings for Accident-Tolerant Fuel Cladding in Light Water Reactors, JOM 70(2) (2018) 248-248.

[13] D.J. Young, Chapter 11 - Effects of Water Vapour on Oxidation, in: D.J. Young (Ed.), High Temperature Oxidation and Corrosion of Metals (Second Edition), Elsevier2016, pp. 549-601.

[14] J. Krejci, M. Sevecek, J. Kabátová, F. Manoch, J. Kočí, P. Bublíková, P. Halodova, H. Namburi, Experimental behavior of chromium-based coatings, TopFuel 2018, Prague, Czech Republic, 2018.

[15] P. Ashcheulov, R. Škoda, J. Škarohlíd, A. Taylor, L. Fekete, F. Fendrych, R. Vega, L. Shao, L. Kalvoda, S. Vratislav, V. Cháb, K. Horáková, K. Kůsová, L. Klimša, J. Kopeček, P. Sajdl, J. Macák, S. Johnson, I. Kratochvílová, Thin polycrystalline diamond films protecting zirconium alloys surfaces: From technology to layer analysis and application in nuclear facilities, Applied Surface Science 359 (2015) 621-628.

[16] M.R. Etty Mutiara, Dip Coating Process of Zircaloy-2 fuel cladding with colloidal graphite, Urania 23(1) (2017) 1-10.

[17] W. Zhong, P.A. Mouche, X. Han, B.J. Heuser, K.K. Mandapaka, G.S. Was, Performance of iron–chromium–aluminum alloy surface coatings on Zircaloy 2 under high-temperature steam and normal BWR operating conditions, Journal of Nuclear Materials 470 (2016) 327-338.

[18] J.-M. Kim, T.-H. Ha, I.-H. Kim, H.-G. Kim, Microstructure and Oxidation Behavior of CrAl Laser-Coated Zircaloy-4 Alloy, 2017.

[19] M.A. Tunes, V.M. Vishnyakov, S.E. Donnelly, Synthesis and characterisation of high-entropy alloy thin films as candidates for coating nuclear fuel cladding alloys, Thin Solid Films 649 (2018) 115-120.

[20] S. Rezaee, G.R. Rashed, M.A. Golozar, Electrochemical and Oxidation Behavior of Yttria Stabilized Zirconia Coating on Zircaloy-4 Synthesized via Sol-Gel Process, International Journal of Corrosion 2013 (2013) 9.

[21] F. Khatkhatay, L. Jiao, J. Jian, W. Zhang, Z. Jiao, J. Gan, H. Zhang, X. Zhang, H. Wang, Superior corrosion resistance properties of TiN-based coatings on Zircaloy tubes in supercritical water, Journal of Nuclear Materials 451(1) (2014) 346-351.

[22] E. Alat, A.T. Motta, R.J. Comstock, J.M. Partezana, D.E. Wolfe, Ceramic coating for corrosion (c3) resistance of nuclear fuel cladding, Surface and Coatings Technology 281 (2015) 133-143.

[23] E. Alat, A.T. Motta, R.J. Comstock, J.M. Partezana, D.E. Wolfe, Multilayer (TiN, TiAlN) ceramic coatings for nuclear fuel cladding, Journal of Nuclear Materials 478 (2016) 236-244.

[24] K. Daub, R. Van Nieuwenhove, H. Nordin, Investigation of the impact of coatings on corrosion and hydrogen uptake of Zircaloy-4, Journal of Nuclear Materials 467 (2015) 260-270.

[25] H. Yeom, B. Hauch, G. Cao, B. Garcia-Diaz, M. Martinez-Rodriguez, H. Colon-Mercado, L. Olson, K. Sridharan, Laser surface annealing and characterization of Ti_2AlC plasma vapor deposition coating on zirconium-alloy substrate, Thin Solid Films 615 (2016) 202-209.

[26] B.R. Maier, B.L. Garcia-Diaz, B. Hauch, L.C. Olson, R.L. Sindelar, K. Sridharan, Cold spray deposition of Ti_2AlC coatings for improved nuclear fuel cladding, Journal of Nuclear Materials 466 (2015) 712-717.

[27] C. Tang, M. Steinbrueck, M. Grosse, S. Ulrich, M. Stueber, H.J. Seifert, Evaluation of magnetron sputtered protective Zr-C-Al coatings for accident tolerant Zircaloy claddings, Proceedings of Water Reactor Fuel Performance Meeting, Jeju Island, Korea, 2017.

[28] J. Ward, D. Bowden, E. Prestat, S. Holdsworth, D. Stewart, M.W. Barsoum, M. Preuss, P. Frankel, Corrosion performance of Ti_3SiC_2, Ti_3AlC_2, Ti_2AlC and Cr_2AlC MAX phases in simulated primary water conditions, Corrosion Science 139 (2018) 444-453.

[29] J. Ward, S. Middleburgh, M. Topping, A. Garner, D. Stewart, M.W. Barsoum, M. Preuss, P. Frankel, Crystallographic evolution of MAX phases in proton irradiating environments, Journal of Nuclear Materials 502 (2018) 220-227.

[30] J. Wang, S. Liu, D. Ren, T. Shao, P. Eklund, R. Huang, Y. Zhu, F. Huang, S. Du, Z. Wang, J. Xue, Y. Wang, Q. Huang, Microstructural evolution of epitaxial Ti_3AlC_2 film on sapphire under ion irradiation and nanoindentation-induced deformation, Journal of Nuclear Materials 509 (2018) 181-187.

[31] M.W. Barsoum, M. Radovic, Elastic and Mechanical Properties of the MAX Phases, Annual Review of Materials Research 41(1) (2011) 195-227.

[32] Z.M. Sun, Progress in research and development on MAX phases: a family of layered ternary compounds, International Materials Reviews 56(3) (2013) 143-166.

[33] P. Eklund, M. Beckers, U. Jansson, H. Högberg, L. Hultman, The $M_{n+1}AX_n$ phases: Materials science and thin-film processing, Thin Solid Films 518(8) (2010) 1851-1878.

[34] J. Gonzalez-Julian, T. Go, D.E. Mack, R. Vaßen, Environmental resistance of Cr_2AlC MAX phase under thermal gradient loading using a burner rig, Journal of the American Ceramic Society 101(5) (2018) 1841-1846.

[35] D.J. Tallman, B. Anasori, M.W. Barsoum, A Critical Review of the Oxidation of Ti_2AlC, Ti_3AlC_2 and Cr_2AlC in Air, Materials Research Letters 1(3) (2013) 115-125.

[36] E.J. Opila, Volatility of Common Protective Oxides in High-Temperature Water Vapor: Current Understanding and Unanswered Questions, Materials Science Forum 461-464 (2004) 765-774.

[37] D. Caplan, M. Cohen, High Temperature Oxidation of Chromium-Nickel Steels, CORROSION 15(3) (1959) 57-62.

[38] O. Berger, R. Boucher, Crack healing in Y-doped Cr_2AlC-MAX phase coatings, Surface Engineering 33(3) (2017) 192-203.

[39] H.J. Yang, X.H. Shao, Y.T. Pei, Z.F. Zhang, J.T.M. De Hosson, Enhanced efficiency of self-healing of Cr2AlC, Materials Letters 227 (2018) 51-54.

[40] R. Pei, S.A. McDonald, L. Shen, S. van der Zwaag, W.G. Sloof, P.J. Withers, P.M. Mummery, Crack healing behaviour of Cr_2AlC MAX phase studied by X-ray tomography, Journal of the European Ceramic Society 37(2) (2017) 441-450.

[41] D.J. Tallman, L. He, J. Gan, E.a.N. Caspi, E.N. Hoffman, M.W. Barsoum, Effects of neutron irradiation of Ti_3SiC_2 and Ti_3AlC_2 in the 121–1085 °C temperature range, Journal of Nuclear Materials 484 (2017) 120-134.

[42] X.M. Liu, M. Le Flem, J.L. Béchade, I. Monnet, Nanoindentation investigation of heavy ion irradiated $Ti_3(Si,Al)C_2$, Journal of Nuclear Materials 401(1-3) (2010) 149-153.

[43] K.R. Whittle, M.G. Blackford, R.D. Aughterson, S. Moricca, G.R. Lumpkin, D.P. Riley, N.J. Zaluzec, Radiation tolerance of $M_{n+1}AX_n$ phases, Ti_3AlC_2 and Ti_3SiC_2, Acta Materialia 58(13) (2010) 4362-4368.

[44] M. Bugnet, V. Mauchamp, E. Oliviero, M. Jaouen, T. Cabioc'h, Chemically sensitive amorphization process in the nanolaminated Cr_2AC (A=Al or Ge) system from TEM in situ irradiation, Journal of Nuclear Materials 441(1) (2013) 133-137.

[45] C. Wang, Z. Han, R. Su, J. Gao, L. Shi, Effects of irradiation damage on the structure in Cr_2AlC thin film, Nuclear Instruments and Methods in Physics Research Section B: Beam Interactions with Materials and Atoms 450 (2019) 286-290.

[46] Q. Huang, H. Han, R. Liu, G. Lei, L. Yan, J. Zhou, Q. Huang, Saturation of ion irradiation effects in MAX phase Cr_2AlC, Acta Materialia 110 (2016) 1-7.

[47] C. Wang, T. Yang, J. Xiao, S. Liu, J. Xue, Q. Huang, J. Zhang, J. Wang, Y. Wang, Structural Transitions Induced by Ion Irradiation in V_2AlC and Cr_2AlC, Journal of the American Ceramic Society 99(5) (2016) 1769-1777.

[48] J. Xiao, T. Yang, C. Wang, J. Xue, Y. Wang, Investigations on Radiation Tolerance of $M_{n+1}AX_n$ Phases: Study of Ti_3SiC_2, Ti_3AlC_2, Cr_2AlC, Cr_2GeC, Ti_2AlC, and Ti_2AlN, Journal of the American Ceramic Society 98(4) (2015) 1323-1331.

[49] D.J. Tallman, E.N. Hoffman, E.a.N. Caspi, B.L. Garcia-Diaz, G. Kohse, R.L. Sindelar, M.W. Barsoum, Effect of neutron irradiation on select MAX phases, Acta Materialia 85 (2015) 132-143.

[50] D.J. Tallman, L. He, B.L. Garcia-Diaz, E.N. Hoffman, G. Kohse, R.L. Sindelar, M.W. Barsoum, Effect of neutron irradiation on defect evolution in Ti_3SiC_2 and Ti_2AlC, Journal of Nuclear Materials 468 (2016) 194-206.

[51] Y. Li, G. Zhao, Y. Qian, J. Xu, M. Li, Deposition of Phase-pure Cr_2AlC Coating by DC Magnetron Sputtering and Post Annealing Using Cr-Al-C Targets with Controlled Elemental Composition but Different Phase Compositions, Journal of Materials Science & Technology (2017).

[52] J. Liu, X. Zuo, Z. Wang, L. Wang, X. Wu, P. Ke, A. Wang, Fabrication and mechanical properties of high purity of Cr_2AlC coatings by adjustable Al contents, Journal of Alloys and Compounds 753 (2018) 11-17.

[53] M. Naveed, A. Obrosov, A. Zak, W. Dudzinski, A. Volinsky, S. Weiß, Sputtering Power Effects on Growth and Mechanical Properties of Cr_2AlC MAX Phase Coatings, Metals 6(11) (2016) 265.

[54] Z. Feng, P. Ke, A. Wang, Preparation of Ti_2AlC MAX Phase Coating by DC Magnetron Sputtering Deposition and Vacuum Heat Treatment, Journal of Materials Science & Technology 31(12) (2015) 1193-1197.

[55] O. Berger, C. Leyens, S. Heinze, R. Boucher, M. Ruhnow, Characterization of Cr–Al–C and Cr–Al–C–Y films synthesized by High Power Impulse Magnetron Sputtering at a low deposition temperature, Thin Solid Films 580 (2015) 6-11.

[56] J.J. Li, Y.H. Qian, D. Niu, M.M. Zhang, Z.M. Liu, M.S. Li, Phase formation and microstructure evolution of arc ion deposited Cr_2AlC coating after heat treatment, Applied Surface Science 263 (2012) 457-464.

[57] J. Rosén, L. Ryves, P.O.Å. Persson, M.M.M. Bilek, Deposition of epitaxial Ti_2AlC thin films by pulsed cathodic arc, Journal of Applied Physics 101(5) (2007) 056101.

[58] C. Tang, M. Klimenkov, U. Jaentsch, H. Leiste, M. Rinke, S. Ulrich, M. Steinbrück, H.J. Seifert, M. Stueber, Synthesis and characterization of Ti_2AlC coatings by magnetron sputtering from three elemental targets and ex-situ annealing, Surface and Coatings Technology 309 (2017) 445-455.

[59] Z. Wang, J. Liu, L. Wang, X. Li, P. Ke, A. Wang, Dense and high-stability Ti_2AlN MAX phase coatings prepared by the combined cathodic arc/sputter technique, Applied Surface Science 396 (2017) 1435-1442.

[60] W. Li, Z. Wang, J. Shuai, B. Xu, A. Wang, P. Ke, A high oxidation resistance Ti2AlC coating on Zirlo substrates for loss-of-coolant accident conditions, Ceramics International 45(11) (2019) 13912-13922.

[61] D. Gilbon, A. Soniak, S. Doriot, J.P. Mardon, Irradiation creep and growth behavior, and microstructural evolution of advanced Zr-base alloys, ASTM Special Technical Publication, ASTM, Toronto, 2000, pp. 51-73.

[62] A. Obrosov, R. Gulyaev, A. Zak, M. Ratzke, M. Naveed, W. Dudzinski, S. Weiß, Chemical and Morphological Characterization of Magnetron Sputtered at Different Bias Voltages Cr-Al-C Coatings, Materials 10(2) (2017) 156.

[63] M.R. Field, P. Carlsson, P. Eklund, J.G. Partridge, D.G. McCulloch, D.R. McKenzie, M.M.M. Bilek, A combinatorial comparison of DC and high power impulse magnetron sputtered Cr_2AlC, Surface and Coatings Technology 259 (2014) 746-750.

[64] J.J. Li, L.F. Hu, F.Z. Li, M.S. Li, Y.C. Zhou, Variation of microstructure and composition of the Cr_2AlC coating prepared by sputtering at 370 and 500°C, Surface and Coatings Technology 204(23) (2010) 3838-3845.

[65] C. Walter, D.P. Sigumonrong, T. El-Raghy, J.M. Schneider, Towards large area deposition of Cr_2AlC on steel, Thin Solid Films 515(2) (2006) 389-393.

[66] C. Tang, M. Steinbrück, M. Große, S. Ulrich, M. Stueber, H. Juergen Seifert, Improvement of the High-Temperature Oxidation Resistance of Zr Alloy Cladding by Surface Modification with Aluminum-Containing Ternary Carbide Coatings, The 2018 International Congress on Advances in Nuclear Power Plants, Charlotte, North Carolina, 2018.

[67] A. Abdulkadhim, M.t. Baben, T. Takahashi, V. Schnabel, M. Hans, C. Polzer, P. Polcik, J.M. Schneider, Crystallization kinetics of amorphous Cr_2AlC thin films, Surface and Coatings Technology 206(4) (2011) 599-603.

[68] R. Grieseler, B. Hähnlein, M. Stubenrauch, T. Kups, M. Wilke, M. Hopfeld, J. Pezoldt, P. Schaaf, Nanostructured plasma etched, magnetron sputtered nanolaminar Cr_2AlC MAX phase thin films, Applied Surface Science 292 (2014) 997-1001.

[69] J. Bohlmark, M. Lattemann, J.T. Gudmundsson, A.P. Ehiasarian, Y. Aranda Gonzalvo, N. Brenning, U. Helmersson, The ion energy distributions and ion flux composition from a high power impulse magnetron sputtering discharge, Thin Solid Films 515(4) (2006) 1522-1526.

[70] A. Ferrec, J. Keraudy, S. Jacq, F. Schuster, P.Y. Jouan, M.A. Djouadi, Correlation between mass-spectrometer measurements and thin film characteristics using dcMS and HiPIMS discharges, Surface and Coatings Technology 250 (2014) 52-56.

[71] Y. Jiang, S. Mráz, J.M. Schneider, Growth of V–Al–C thin films by direct current and high power impulse magnetron sputtering from a powder metallurgical composite target, Thin Solid Films 538 (2013) 1-6.

[72] H. Elmkhah, F. Attarzadeh, A. Fattah-alhosseini, K.H. Kim, Microstructural and electrochemical comparison between TiN coatings deposited through HIPIMS and DCMS techniques, Journal of Alloys and Compounds 735 (2018) 422-429.

[73] H. Hoche, S. Groß, M. Oechsner, Development of new PVD coatings for magnesium alloys with improved corrosion properties, Surface and Coatings Technology 259 (2014) 102-108.

[74] A.P. Ehiasarian, P.E. Hovsepian, L. Hultman, U. Helmersson, Comparison of microstructure and mechanical properties of chromium nitride-based coatings deposited by high power impulse magnetron sputtering and by the combined steered cathodic arc/unbalanced magnetron technique, Thin Solid Films 457(2) (2004) 270-277.

[75] D.V. Shtansky, P.V. Kiryukhantsev-Korneev, A.N. Sheveyko, B.N. Mavrin, C. Rojas, A. Fernandez, E.A. Levashov, Comparative investigation of TiAlC(N), TiCrAlC(N), and CrAlC(N) coatings deposited by sputtering of MAX-phase $Ti_{2-x}Cr_xAlC$ targets, Surface and Coatings Technology 203(23) (2009) 3595-3609.

[76] V. Consonni, G. Feuillet, P. Gergaud, Plasticity induced texture development in thick polycrystalline CdTe: Experiments and modeling, Journal of Applied Physics 103(6) (2008) 063529.

[77] J. Wang, Y. Zhou, Z. Lin, F. Meng, F. Li, Raman active phonon modes and heat capacities of Ti_2AlC and Cr_2AlC ceramics: first-principles and experimental investigations, Applied Physics Letters 86(10) (2005) 101902.

[78] O.D. Leaffer, S. Gupta, M.W. Barsoum, J.E. Spanier, On Raman scattering from selected M_2AC compounds, Journal of Materials Research 22(10) (2011) 2651-2654.

[79] V. Vishnyakov, O. Crisan, P. Dobrosz, J.S. Colligon, Ion sputter-deposition and in-air crystallisation of Cr_2AlC films, Vacuum 100 (2014) 61-65.

[80] R. Su, H. Zhang, X. Meng, L. Shi, C. Liu, Synthesis of Cr_2AlC thin films by reactive magnetron sputtering, Fusion Engineering and Design 125 (2017) 562-566.

[81] J. Spanier, S. Gupta, M. Amer, M. Barsoum, Vibrational behavior of the $M_{n+1}AX_n$ phases from first-order Raman scattering (M=Ti,V,Cr, A=Si, X=C,N), 2005.

[82] O. Crisan, A.D. Crisan, Elastic properties and crystallization of thermal barrier coatings of Cr_2AlC, Dig. J. Nanomater. Biostruct. 12(4) (2017) 1165-1174.

[83] G. Neumann, C. Tuijn, Self-diffusion and impurity diffusion in pure metals: handbook of experimental data, Elsevier2011.

[84] S.C. Tjong, Laser raman spectroscopic studies of the surface oxides formed on iron chromium alloys at elevated temperatures, Materials Research Bulletin 18(2) (1983) 157-165.

[85] W.A. England, S.N. Jenny, D.A. Greenhalgh, Chromium oxide film thickness measurements using spontaneous Raman scattering, Journal of Raman Spectroscopy 15(3) (1984) 156-159.

[86] R. Wäsche, G. Brandt, R. Ehrke, G. Nolze, T. Schmid, S. Sasaki, M. Woydt, Wear behaviour of α-alumina in hot steam at high contact pressure, Wear 404-405 (2018) 22-30.

[87] H.D. Ruan, R.L. Frost, J.T. Kloprogge, Comparison of Raman spectra in characterizing gibbsite, bayerite, diaspore and boehmite, Journal of Raman Spectroscopy 32(9) (2001) 745-750.

[88] R.S. Krishnan, Raman Spectrum of Alumina and the Luminescence and Absorption Spectra of Ruby, Nature 160(4053) (1947) 26-26.

[89] S.P.S. Porto, R.S. Krishnan, Raman Effect of Corundum, The Journal of Chemical Physics 47(3) (1967) 1009-1012.

[90] A. Misra, H.D. Bist, M.S. Navati, R.K. Thareja, J. Narayan, Thin film of aluminum oxide through pulsed laser deposition: a micro-Raman study, Materials Science and Engineering: B 79(1) (2001) 49-54.

[91] C. Duriez, T. Dupont, B. Schmet, F. Enoch, Zircaloy-4 and M5® high temperature oxidation and nitriding in air, Journal of Nuclear Materials 380(1) (2008) 30-45.

[92] M. Steinbrück, N. Vér, High-temperature oxidation of Zircaloy-4 in mixed steam-air and steam-nitrogen atmospheres, International Congress on Advances in Nuclear Power Plants 2010, ICAPP 2010, 2010, pp. 1051-1061.

[93] M. Steinbrueck, F.O. da Silva, M. Grosse, Oxidation of Zircaloy-4 in steam-nitrogen mixtures at 600–1200 °C, Journal of Nuclear Materials 490 (2017) 226-237.

[94] M. Negyesi, M. Amaya, Oxidation kinetics of Zry-4 fuel cladding in mixed steam–air atmospheres at temperatures of 1273–1473 K, Journal of Nuclear Science and Technology 54(10) (2017) 1143-1155.

[95] A. Michau, F. Maury, F. Schuster, F. Lomello, J.C. Brachet, E. Rouesne, M. Le Saux, R. Boichot, M. Pons, High-temperature oxidation resistance of chromium-based coatings deposited by DLI-MOCVD for enhanced protection of the inner surface of long tubes, Surface and Coatings Technology 349 (2018) 1048-1057.

[96] O. Berger, Part I - Mechanism of oxidation of Cr_2AlC films in temperature range 700-1200°C, Surface Engineering 31(5) (2015) 373-385.

[97] J. Fu, T.F. Zhang, Q. Xia, S.-H. Lim, Z. Wan, T.-W. Lee, K.H. Kim, Oxidation and Corrosion Behavior of Nanolaminated MAX-Phase Ti_2AlC Film Synthesized by High-Power Impulse Magnetron Sputtering and Annealing, Journal of Nanomaterials 2015 (2015) 1-12.

[98] Z.J. Lin, M.S. Li, J.Y. Wang, Y.C. Zhou, High-temperature oxidation and hot corrosion of Cr_2AlC, Acta Materialia 55(18) (2007) 6182-6191.

[99] D.B. Lee, S.W. Park, Oxidation of Cr_2AlC Between 900 and 1200°C in Air, Oxidation of Metals 68(5-6) (2007) 211-222.

[100] W. Tian, P. Wang, Y. Kan, G. Zhang, Oxidation behavior of Cr_2AlC ceramics at 1,100 and 1,250 °C, Journal of Materials Science 43(8) (2008) 2785-2791.

[101] D.B. Lee, T.D. Nguyen, J.H. Han, S.W. Park, Oxidation of Cr_2AlC at 1300°C in air, Corrosion Science 49(10) (2007) 3926-3934.

[102] Q.M. Wang, R. Mykhaylonka, A. Flores Renteria, J.L. Zhang, C. Leyens, K.H. Kim, Improving the high-temperature oxidation resistance of a β–γ TiAl alloy by a Cr_2AlC coating, Corrosion Science 52(11) (2010) 3793-3802.

[103] D.E. Hajas, M. to Baben, B. Hallstedt, R. Iskandar, J. Mayer, J.M. Schneider, Oxidation of Cr_2AlC coatings in the temperature range of 1230 to 1410°C, Surface and Coatings Technology 206(4) (2011) 591-598.

[104] Z.J. Lin, Y.C. Zhou, M.S. Li, Synthesis, microstructure, and property of Cr_2AlC, Journal of Materials Science & Technology 23(6) (2007) 721-746.

[105] Z. Lin, M. Zhuo, Y. Zhou, M. Li, J. Wang, Atomic scale characterization of layered ternary Cr_2AlC ceramic, Journal of Applied Physics 99(7) (2006) 076109.

[106] M. Bugnet, M. Jaouen, V. Mauchamp, T. Cabioc'h, G. Hug, Experimental and first-principles investigation of the electronic structure anisotropy of Cr_2AlC, Physical Review B 90(19) (2014) 195116.

[107] W.F. Chu, A. Rahmel, The conversion of chromium oxide to chromium carbide, Oxidation of Metals 15(3) (1981) 331-337.

[108] R.F. Voitovich, É.A. Pugach, High-temperature oxidation characteristics of the carbides of the Group VI transition metals, Soviet Powder Metallurgy and Metal Ceramics 12(4) (1973) 314-318.

[109] Ş. Şen, O. Ozdemir, A.S. Demirkıran, U. Şen, Oxidation Kinetics of Chromium Carbide Coating Produced on AISI 1040 Steel by Thermo-Reactive Deposition Method during High Temperature in Air, Advanced Materials Research 445 (2012) 649-654.

[110] M. Backhaus-Ricoult, Oxidation Behavior of SiC-Whisker-Reinforced Alumina-Zirconia Composites, Journal of the American Ceramic Society 74(8) (1991) 1793-1802.

[111] K.L. Luthra, H.D. Park, Oxidation of Silicon Carbide-Reinforced Oxide-Matrix Composites at 1375° to 1575°C, Journal of the American Ceramic Society 73(4) (1990) 1014-1023.

[112] C.T. Fu, J.M. Wu, Oxidation behavior of electroconductive Al_2O_3-Cr_3C_2 composites, Br. Ceram. Trans. 94(3) (1995) 112-117.

[113] S.R.J. Saunders, M. Monteiro, F. Rizzo, The oxidation behaviour of metals and alloys at high temperatures in atmospheres containing water vapour: A review, Progress in Materials Science 53(5) (2008) 775-837.

[114] A.-S. Farle, C. Kwakernaak, S. van der Zwaag, W.G. Sloof, A conceptual study into the potential of $M_{n+1}AX_n$ phase ceramics for self-healing of crack damage, Journal of the European Ceramic Society 35(1) (2015) 37-45.

[115] W.G. Sloof, R. Pei, S.A. McDonald, J.L. Fife, L. Shen, L. Boatemaa, A.S. Farle, K. Yan, X. Zhang, S. van der Zwaag, P.D. Lee, P.J. Withers, Repeated crack healing in MAX-phase ceramics revealed by 4D in situ synchrotron X-ray tomographic microscopy, Sci Rep 6 (2016) 23040.

List of figure captions

Fig. 1: (a) Comparison of the X-ray diffraction (XRD) patterns for Cr_2AlC target and 3.2 µm thick as-deposited and annealed coatings on a Zr702. Cr_2AlC peaks are indexed with the PDF-00-058-0267 card. (b) Comparison of the µRaman for Cr_2AlC target, as-deposited and annealed coatings on a Zr702.

Fig. 2: (a) SEM image in Secondary Electron (SE) mode of a fractured cross-section of as-deposited Cr-Al-C coating on Si. (b) SEM image in Backscattered electron (BSE) mode of the cross-section of annealed Cr_2AlC coating on Zr702 after 4 h at 823 K in Ar.

Fig. 3: XRD patterns (a) and Raman spectra (b) of oxidized 3.2 µm thick as-deposited Cr-Al-C and annealed Cr_2AlC coatings on Zr702. Reaction conditions: 15 min at 1373 K in static air.

Fig. 4: Overlay of GDOES composition profiles and SEM-BSE cross-sections of oxidized 3.2 µm thick as-deposited Cr-Al-C (a) and annealed Cr_2AlC (b) coatings on Zr702. Reaction conditions: 15 min at 1373 K in static air.

Fig. 5: SEM-BSE images of cross-sections at various magnifications of an oxidized 3.2 µm thick as-deposited Cr-Al-C coating on Zr702 at a submicronic crack (a, b), and a larger defect (c, d). Reaction conditions: 15 min at 1373 K in static air.

Fig. 6: XRD patterns of a 3.2 µm thick annealed Cr_2AlC coating on Zr702 oxidized at 1373 K in static air during 15, 30 and 60 minutes.

Fig. 7: (a-c) SEM-SE cross-sections images of an annealed Cr_2AlC coating (~ 3 µm) after an oxidation at 1373 K in static air for 15 min (a) and 60 min (b,c). (d-f) SEM-SE cross-sections images of a Cr coating (~ 15 µm) after oxidation at 1373 K in static air for 15 min (d) and 60 min (e, f).

Fig. 8: Thermogravimetric analysis (TGA) TGA of uncoated and coated Zr702 substrates (as-deposited Cr-Al-C (7 µm) and Cr (15 µm) under dry (solid curves) and wet air (dotted curves) during the heating ramp and the isothermal oxidation at 1473 K for 10 min.

Fig. 9: Overlay of GDOES composition profiles and SEM-BSE cross-sections of oxidized 7 µm thick as-deposited Cr-Al-C coating on Zr702. Oxidation conditions: 120 min at 1473 K in wet air.

List of figures

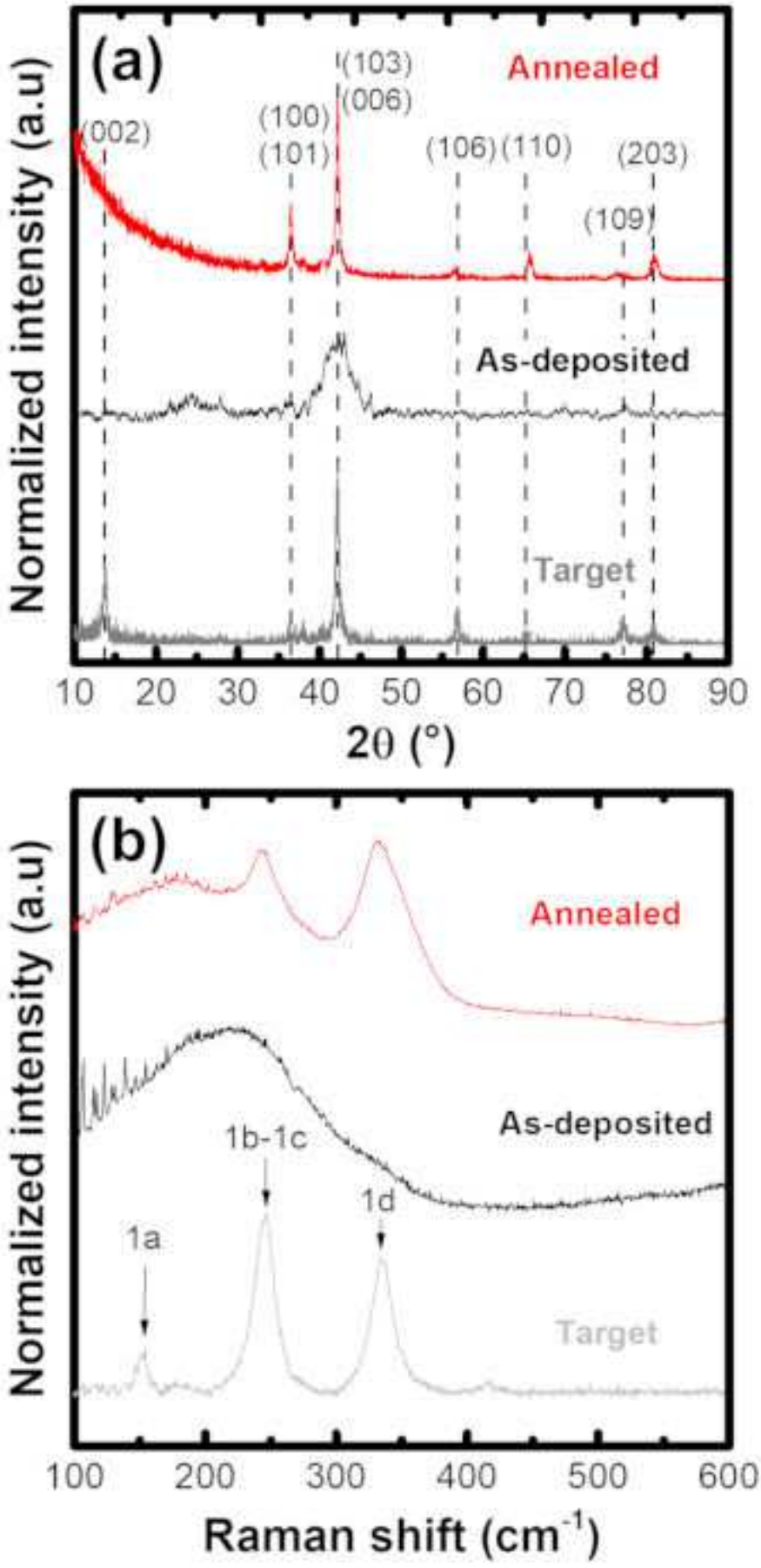

Figure 1

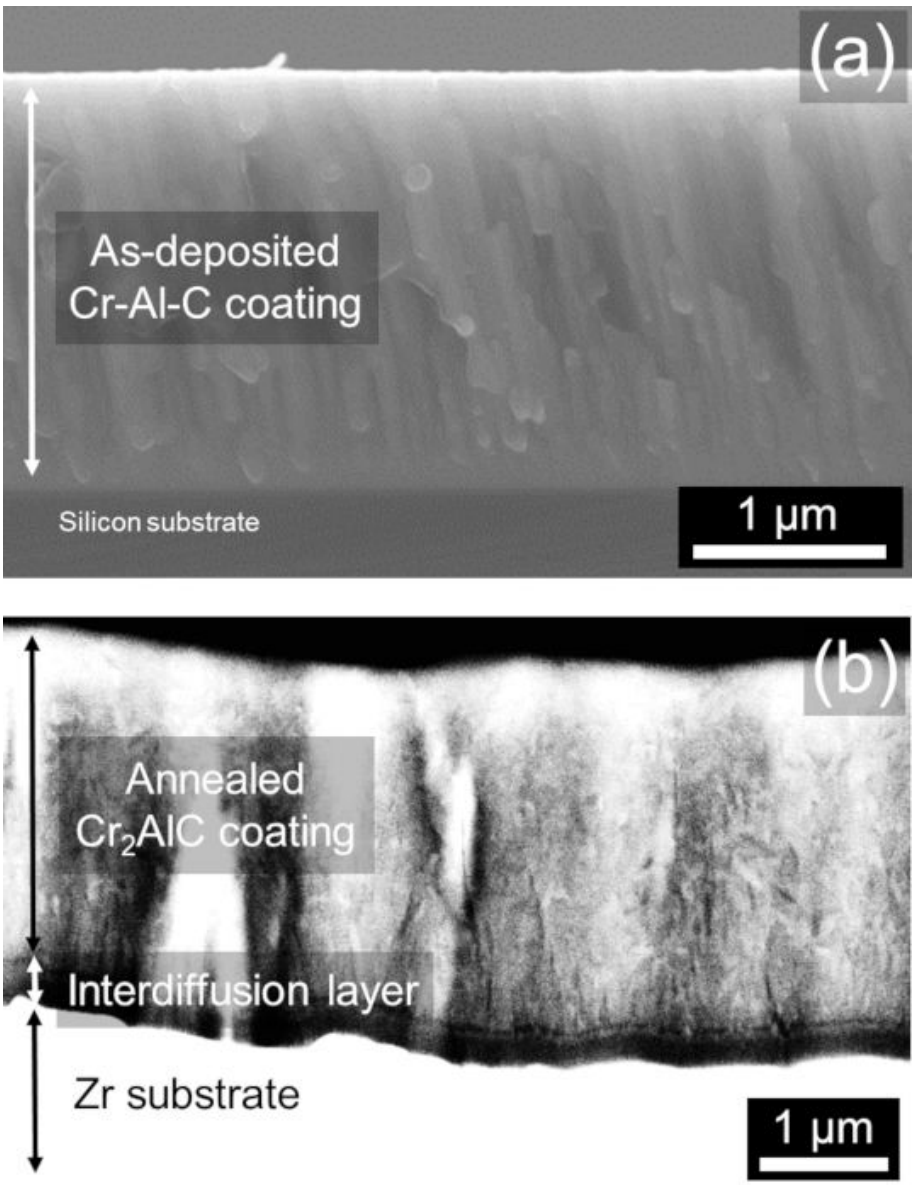
(a)
As-deposited
Cr-Al-C coating
Silicon substrate
1 μm
(b)
Annealed
Cr2AlC coating
Interdiffusion layer
Zr substrate
1 μm

Figure 2

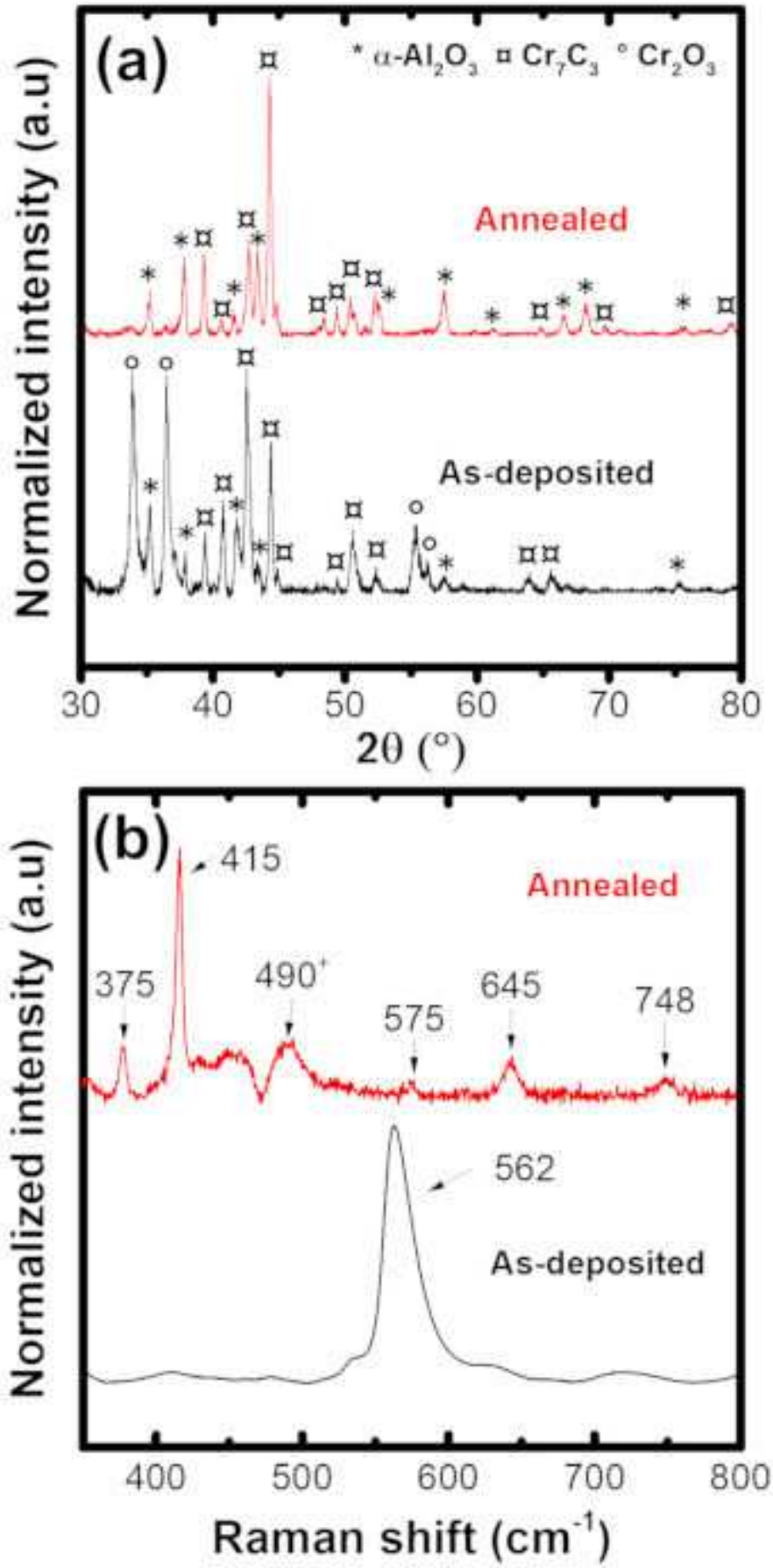
(a)
* α-Al2O3 ¤ Cr7C3 ° Cr2O3
Annealed
As-deposited
Normalized intensity (a.u)
30
40
50
60
70
80
2θ (°)
(b)
415
Annealed
375
490
575
645
748
562
As-deposited
Normalized intensity (a.u)
400
500
600
700
800
Raman shift (cm-1)

Figure 3

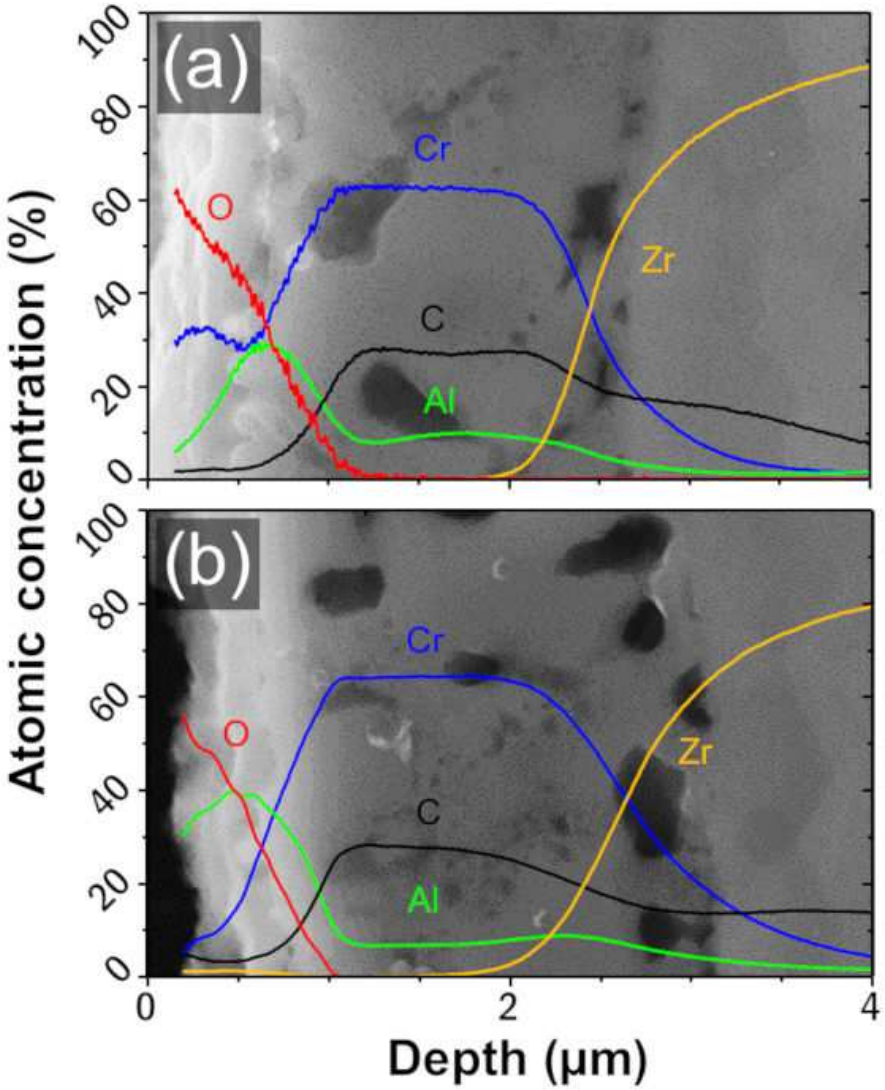
(a)
(b)
Cr
O
C
Al
Zr
Atomic concentration (%)
Depth (μm)
0
20
40
60
80
100
0
2
4

Figure 4

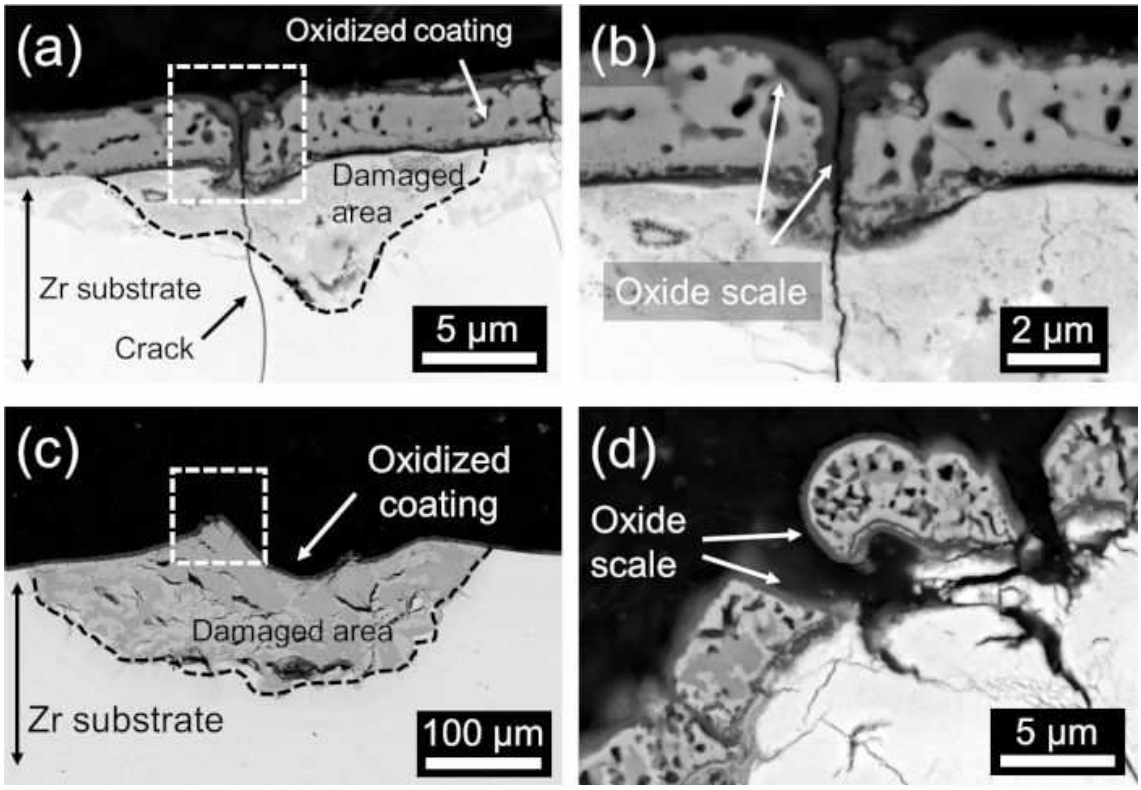
(a)
Oxidized coating
Damaged area
Zr substrate
Crack
5 μm
(b)
Oxide scale
2 μm
(c)
Oxidized coating
Damaged area
Zr substrate
100 μm
(d)
Oxide scale
5 μm
Figure 5

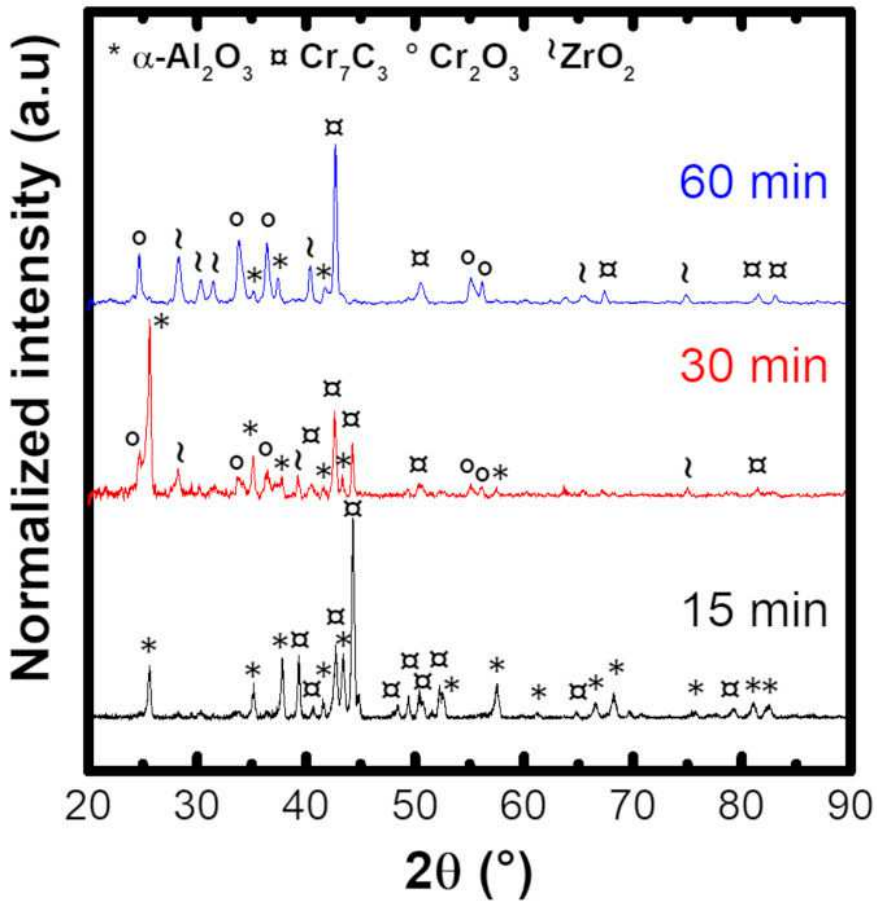
* α-Al2O3 ¤ Cr7C3 ° Cr2O3 ≀ZrO2
60 min
30 min
15 min
Normalized intensity (a.u)
20
30
40
50
60
70
80
90
2θ (°)

Figure 6

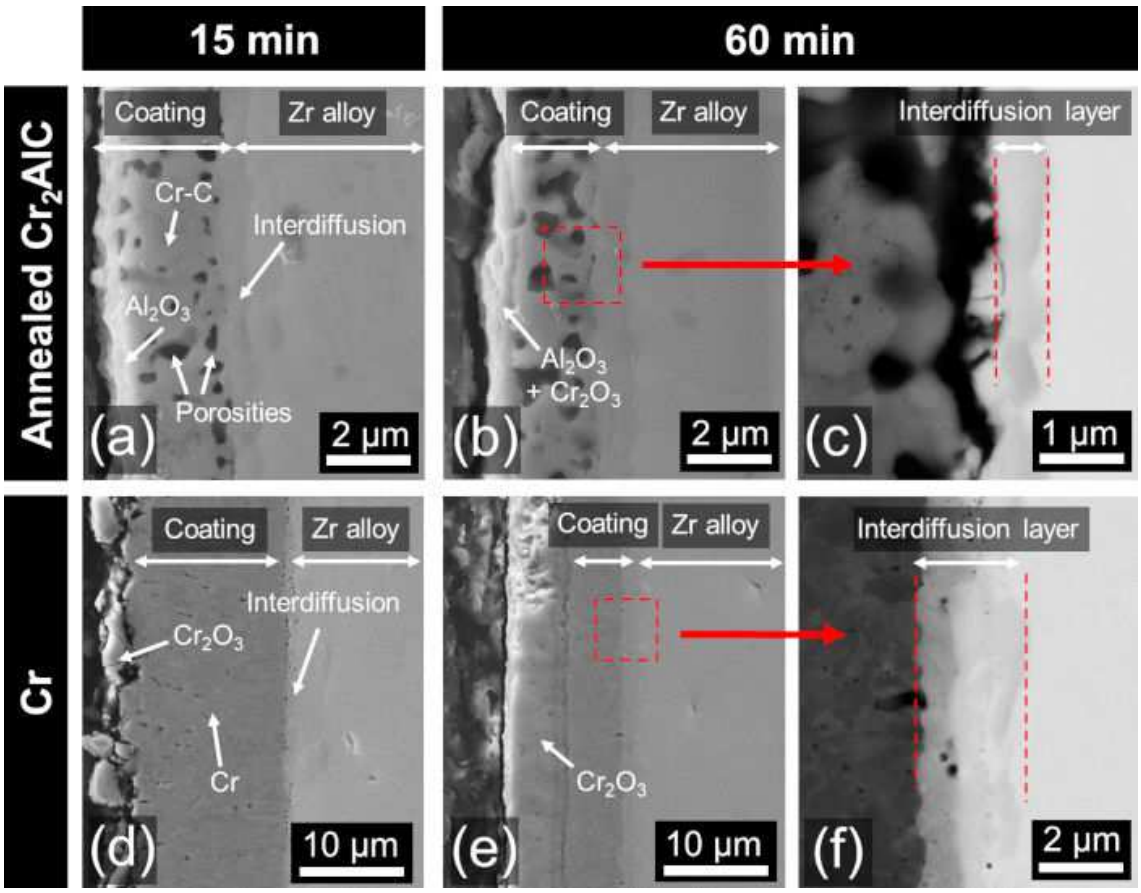
15 min
60 min
Annealed Cr_2AlC
Cr
Coating
Zr alloy
Cr-C
Interdiffusion
Al_2O_3
Porosities
(a)
2 μm
(b)
Al_2O_3 + Cr_2O_3
(c)
Interdiffusion layer
1 μm
Cr_2O_3
Cr
(d)
10 μm
(e)
(f)
2 μm
Figure 7

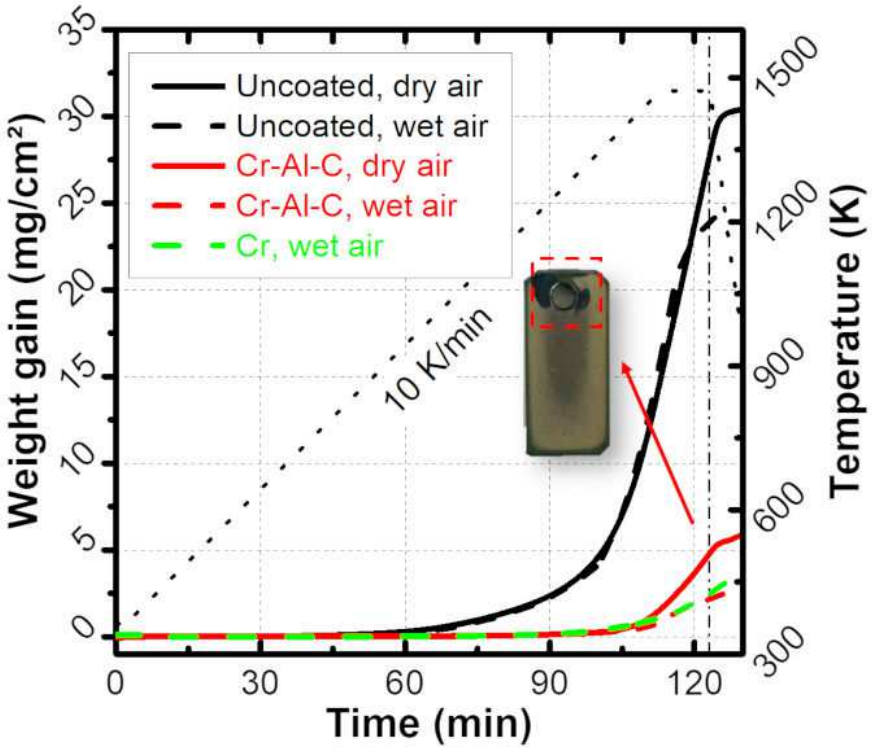
Uncoated, dry air
Uncoated, wet air
Cr-Al-C, dry air
Cr-Al-C, wet air
Cr, wet air
10 K/min
Weight gain (mg/cm²)
Temperature (K)
Time (min)
0
5
10
15
20
25
30
35
300
600
900
1200
1500
0
30
60
90
120

Figure 8

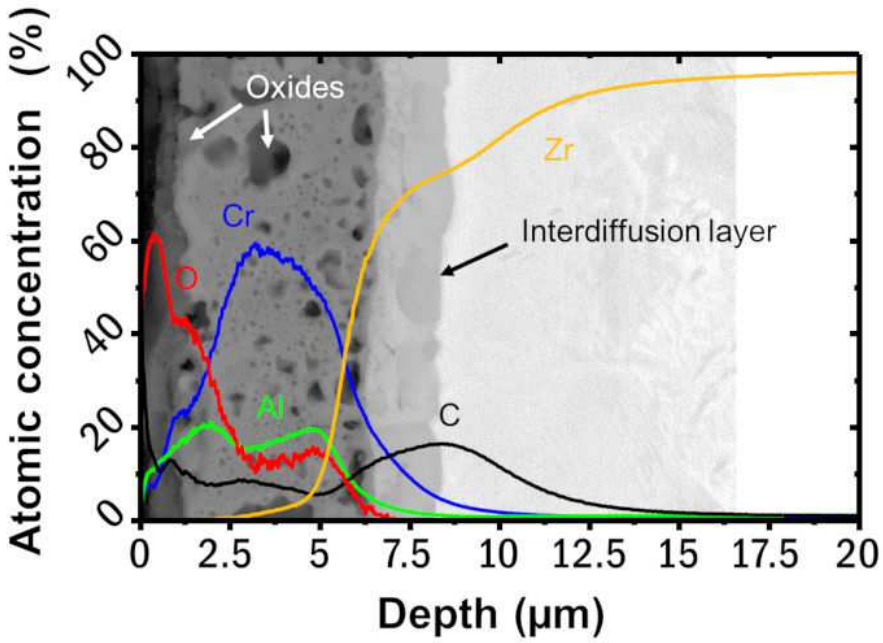
Atomic concentration (%)
100
80
60
40
20
0
Oxides
Cr
O
Al
C
Zr
Interdiffusion layer
0
2.5
5
7.5
10
12.5
15
17.5
20
Depth (μm)

Figure 9